

Structural and magnetodielectric properties of BiFeO₃-GdMnO₃ multiferroics

R. Masso¹, S. N. Tripathy^{2,3}, F. A. Aponte¹, D. K. Pradhan², R. Martinez¹, and R. Palai^{1*}

¹*Department of Physics, University of Puerto Rico, San Juan, PR 00936, USA*

²*Department of Physics and Astronomy, National Institute of Technology (NIT), Rourkela, Odisha, India*

³*Present Address: Department of Physics, Koneru Lakshmaiah Education Foundation, Deemed to be University, Hyderabad, Telangana, India-500075*

(Dated: January 12, 2021)

We report on structural, microstructural, spectroscopic, dielectric, electrical, ferroelectric, ferromagnetic, and magnetodielectric coupling studies of BiFeO₃-GdMnO₃[(BFO)_{1-x}-(GMO)_x], where x is the concentration of GdMnO₃ ($x=0.0, 0.025, 0.05, 0.075, 0.1, 0.15,$ and 0.2), nanocrystalline ceramic solid solutions by auto-combustion method. The analysis of structural property by Rietveld refinement shows the existence of morphotropic phase boundary (MPB) at $x=0.10$, which is in agreement with the Raman spectroscopy and high resolution transmission electron microscopy (HRTEM) studies. The average crystallite size obtained from the transmission electron microscopy (TEM) and X-ray line profile analysis was found to be 20-30 nm. The scanning electron micrographs show the uniform distribution of grains throughout the surface of the sample. The dielectric dispersion behavior fits very well with the Maxwell-Wagner model. The frequency dependent phase angle (θ) study shows the resistive nature of solid solutions at low frequency, whereas it shows capacitive behavior at higher frequencies. The temperature variation of dielectric permittivity shows dielectric anomaly at the magnetic phase transition temperature and shifting of the phase transition towards the lower temperature with increasing GMO concentration. The Nyquist plot showed the conduction mechanism is mostly dominated by grains and grain boundary resistances. The ac conductivity of all the samples follows the modified Jonscher model. The impedance and modulus spectroscopy show a non-Debye type relaxation mechanism which can be modeled using a constant phase element (CPE) in the equivalent circuit. The solid-solutions of BFO-GMO show enhanced ferromagnetic-like behavior at room temperature. The ferroelectric polarization measurement shows lossy ferroelectric behavior. The frequency dependent magnetocapacitance and magnetoimpedance clearly show the existence of intrinsic magnetodielectric coupling. The (BFO)_{1-x}-(GMO)_x solid solutions with $x=0.025-0.075$ show significantly higher magnetocapacitance and magnetoimpedance compared to the pure BFO.

I. INTRODUCTION

Multiferroic materials are attracting a great deal of interest because of their unusual interesting physical properties, such as coexistence of multiple switchable states (polarization, magnetization or strain), magnetoelectric (ME) coupling, structural phase transitions, and their potential applications in secure data storage, spintronics, and novel multifunctional devices [1–8]. The information stored by splitting data in multiferroic memory over two mediums (half stored electrically and half stored magnetically) could be encrypted in such a way that makes it for more secure than is currently possible, which will open up a new era in data storage.

BiFeO₃ (BFO) is a rare Pb-free room temperature (RT) single phase multiferroic (ferroelectric $T_c = 830^\circ\text{C}$ and antiferromagnetic $T_N = 370^\circ\text{C}$ [4–6]. However, high leakage current, weak magnetoelectric coupling, presence of cycloidal spin spiral, and critical structural stability of BFO are the bottlenecks for practical applications [9, 10]. BFO, which is Type-I multiferroics, showed large ferroelectric polarization due to *charge ordering* and displacement of ions because of lattice distortion, but it shows

weak ME coupling. However, in Type-II multiferroics, the polarization is due to certain *magnetic ordering* and is of electronic in origin, but it shows stronger ME coupling than Type-I multiferroics [11]. The objective of this present work is to affect the ferroic orderings of BFO to enhance the ME coupling.

It has been found that solid-solutions of BFO with rare-earth (RE) manganite REMnO₃ (RE= Dy, Sm, La, Gd, Y, *etc.*) [12] can stabilize the crystal structure, reduce the leakage current, suppress the spiral spin structure of BFO, and can facilitate the release of latent magnetization [13, 14]. RE elements show a large net magnetic moment which originates from the electrons of unfilled $4f$ shells due to both orbital and spin magnetic moments. The $4f$ electrons (deep shell) are very localized and shielded by s and p orbitals from other ions in the field. Therefore, the orbital moments of rare earth ions remain unquenched. GdMnO₃ (GMO), a magnetoelectric with an incommensurate antiferromagnetic phase transition at $T_N \sim -230^\circ\text{C}$ (43 K), which is associated with the sinusoidal antiferromagnetic ordering of the Mn³⁺ ions magnetic moment. GMO shows a strong lattice modulation due to the correlation between electric and magnetic orders and strong spin-lattice coupling between Gd $4f$ -spin sublattice with Mn $3d$ spin. As the ME coupling interlinked with spin-charge-lattice interactions, it is expected that the substitution of Gd³⁺ (ef-

*Electronic address: r.palai@upr.edu

fective magnetic moment, $\mu_{\text{eff}} = 7.9\mu_B$) at Bi-site of the BFO can switch off the lone pair activity of Bi leading to shift the ferroelectric phase transition towards closer to (anti)ferromagnetic phase transition and resulting a stronger ME coupling [15].

A strong ME coupling between magnetization (M) and polarization (P) has not been achieved in BFO because of the problem to sustain the high electric field necessary to switch the magnetization. The enhancement in multiferroic properties of BFO has been observed by synthesizing nanoparticles smaller than spin cycloid (60 nm) due to the size effect. In multiferroics, M couples to P and thus to the dielectric constant (ϵ). We propose to study the ME coupling through the magnetodielectric (MD) effect. The dielectric constant relates to the index of the refraction (η) of the material; $\eta = (\mu\epsilon)^{1/2}$, where μ and ϵ are the permeability and permittivity of the material, respectively. The tuning of refractive index by the application of a magnetic field would give rise a novel functionality to magnetoelectric and magneto-optic devices. However, there many unanswered questions need to be addressed: What is the mechanism that gives rise to MD coupling? Why and under what circumstances a large MD coupling should exist and how to control it? What are the effects of temperature, frequency, interface, and electromagnetic field on MD coupling? What is the influence of the strain effect, size effect, and reduced dimensionality on MD coupling? In order to understand and enhance the MD coupling of BFO, we carried out a systematic study of $(\text{BFO})_{1-x}(\text{GMO})_x$ solid-solutions. In this present work, we report on structural, microstructural, spectroscopic, dielectric, electrical, ferroelectric, ferromagnetic, and magnetodielectric properties of $(\text{BFO})_{1-x}(\text{GMO})_x$, where $x = 0.0, 0.025, 0.05, 0.075, 0.1, 0.15,$ and 0.2 , nanocrystalline ceramics by auto-combustion method.

II. EXPERIMENTAL DETAILS

Nanocrystalline ceramic solid solutions of $(\text{BFO})_{1-x}(\text{GMO})_x$ ($0.0 \leq x \leq 0.2$) were synthesized using analytical grade chemicals of $\text{Fe}(\text{NO}_3)_3 \cdot 9\text{H}_2\text{O}$, $\text{Bi}(\text{NO}_3)_3 \cdot 5\text{H}_2\text{O}$, Gd_2O_3 and $(\text{CH}_3\text{COO})_2\text{Mn} \cdot 4\text{H}_2\text{O}$ with urea as a fuel. The homogeneous gel of these reagents were added stoichiometrically to this fuel and later were dissolved in nitric acid and water. The gel was heated to 400°C for 30 min and then the solvent was evaporated and auto-ignited to result in residues that were crushed later. The extracted material from this reaction was milled for homogeneity. The details of the auto-combustion synthesis process are described elsewhere [13, 16, 17]. The combustion residue of different concentration were calcinated at different temperatures for 3 h; for $x=0.0$ at 550°C in air, $0.025 \leq x \leq 0.1$ at 700°C for $x=0.15$ and $x=0.2$ at 750°C . After the calcination, the powder was press to $8 \times 10^7 \text{Kg/m}^2$ in cylindrical pellets utilizing polyvinyl alcohol as binder. The samples with concentration of $0.0 \leq x \leq 0.1$ were sintered at 750°C , while samples with

concentration of $0.15 \leq x \leq 0.2$ were sintered at 780°C , for 6 h. The stoichiometry and phase purity of the samples were studied using X-ray diffraction (XRD) (Philips Analytical-PW3040) at $2^\circ/\text{min}$ from $20^\circ \leq 2\theta \leq 80^\circ$ using $\text{Cu-K}\alpha$ radiation ($\lambda=1.5405\text{\AA}$). X-ray line-profile analysis of the samples was used to calculate the crystallite size and lattice strain in the samples using BREADTH software [18]. Micro-Raman spectra of the samples were recorded on backscattering geometry using the 514.5nm Ar-ion laser line using Renishaw micro-Raman spectrometer (model-INVIA). Microstructure, distribution of grain growth, and particle size were studied using field emission scanning electron microscope (SUPRA 35VT SEM) and transmission electron microscope (Techo C230 STwin TEM). For the electrical characterization, the pellets were polished and electroded with silver paint and dried at 150°C for 3 h. Ferroelectric polarization measurements were carried out using Marine PE loop tracer. Dielectric and magnetodielectric measurements were carried out in a wide range of frequency (100 Hz-1 MHz) with the Hioki 3532-50 LCR meter and in-house ME measurement setup. Magnetic properties were carried out at room temperature using a vibrating sample magnetometer (Lakshore 142AVSM) up to a maximum field of ± 2 T at RT.

III. RESULTS AND DISCUSSION

A. Structural and microstructural properties

Figure 1 shows the XRD pattern of $(\text{BFO})_{1-x}(\text{GMO})_x$ $0.0 \leq x \leq 0.2$ solid-solutions. The XRD pattern of the samples was analyzed using the Rietveld refinement using FULLPROF 2.2.4 package [17]. The calculated and difference pattern with Bragg's position of the peaks were given for comparison. The peak shapes were refined using a pseudo-Voigt function and background was corrected using a six-coefficient polynomial function. In order to get a better refinement, zero correction, scale factor, background, unit cell parameters, atomic positions, thermal parameters, and half width parameters (U , V , and W) were varied. The occupancy of all the atomic sites was kept fixed during the refinement process. Rhombohedral crystal structure of undoped BiFeO_3 in R3c space group was used for Rietveld refinement. From the refinement analysis, it was found that BFO with up to $\leq 7.5\%$ GMO concentration shows single phase with R3c space group, whereas above it shows a mixed phase (R3c + Pn2_{1a}).

As can be seen from Fig. 1, a good agreement (goodness of fit $\chi^2 = 1.15-1.30$) has been observed between the observed and the calculated patterns for all the samples. No traces of impurity phases (*i.e.*, $\text{Bi}_2\text{Fe}_4\text{O}_9$ and $\text{Bi}_{25}\text{FeO}_{39}$) were observed in the samples. The difference between the observed and calculated pattern and the Bragg's positions are given below the observed spectrum (Fig. 1) for comparison. The lattice constant, space

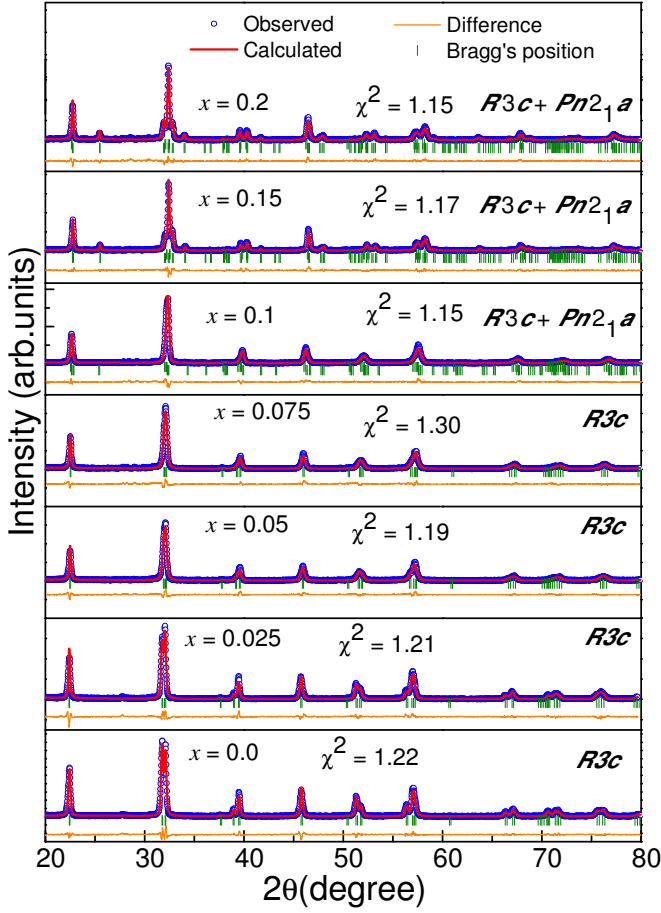


FIG. 1: XRD pattern of $(\text{BFO})_{1-x}(\text{GMO})_x$ $0.0 \leq x \leq 0.2$ solid-solutions. The calculated and difference pattern with Bragg's position of the peaks were given for comparison.

TABLE I: Lattice constant, space group, and goodness of fit (χ^2) obtained from the Rietveld refinement of $(\text{BFO})_{1-x}(\text{GMO})_x$ $0.0 \leq x \leq 0.2$ samples.

| x | Space group | Lattice Parameters A | | | χ^2 |
|-------|-------------------|----------------------|---------|---------|----------|
| | | a | b | c | |
| 0.0 | R3c | 5.5761 | 5.5761 | 13.8685 | 1.22 |
| 0.025 | R3c | 5.5832 | 5.5832 | 13.8615 | 1.21 |
| 0.05 | R3c | 5.5706 | 5.5706 | 13.7837 | 1.19 |
| 0.075 | R3c | 5.5642 | 5.5642 | 13.7568 | 1.30 |
| 0.1 | R3c+ | 5.5551 | 5.5551 | 13.7113 | 1.20 |
| | Pn2 _{1a} | 5.5476 | 7.78937 | 5.54864 | |
| 0.15 | R3c+ | 5.5571 | 5.5571 | 13.4245 | 1.17 |
| | Pn2 _{1a} | 5.5866 | 7.8098 | 5.45706 | |
| 0.2 | R3c+ | 5.5805 | 5.5805 | 13.4504 | 1.15 |
| | Pn2 _{1a} | 5.6010 | 7.8093 | 5.45655 | |

group, and goodness of fit obtained from the Rietveld refinement of $(\text{BFO})_{1-x}(\text{GMO})_x$ $0.0 \leq x \leq 0.2$ samples are given in Table 1.

The existence of both rhombohedral and orthorhombic structure becomes more prominent with increasing x . For $x = 0.2$, the XRD pattern contains the reflections, which are the characteristics of Pnma/Pbnm space

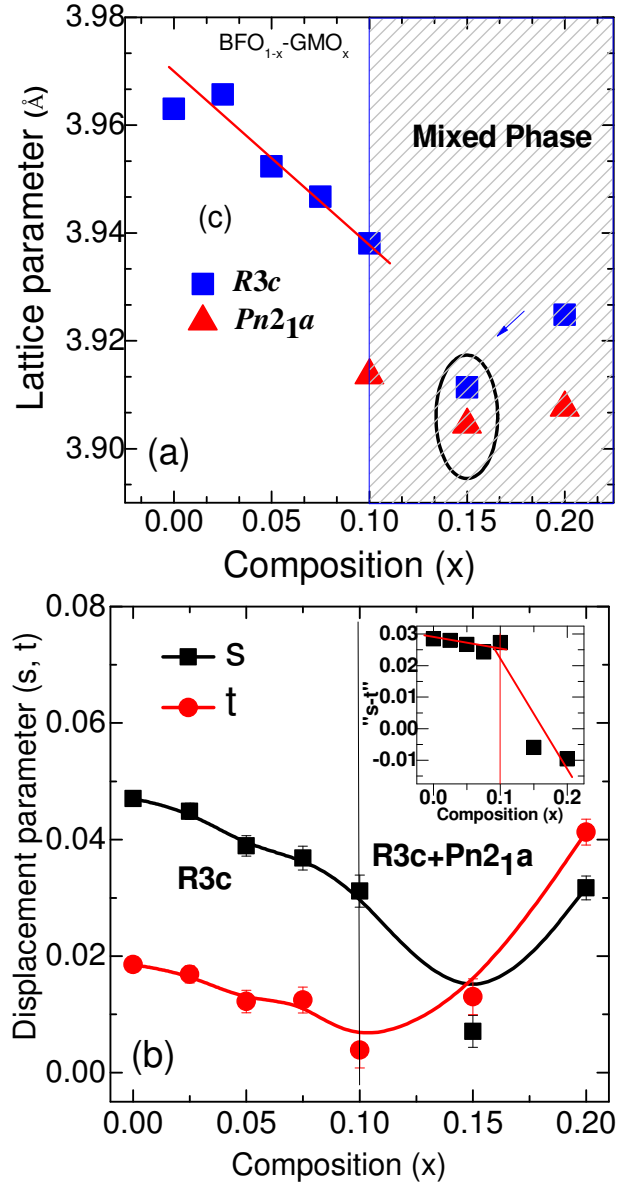


FIG. 2: (a) Pseudo-cubic lattice parameter as a function of composition of $(\text{BFO})_{1-x}(\text{GMO})_x$ $0.0 \leq x \leq 0.2$; (b) Atomic displacement parameters (s , t) as function of composition (Inset-Compositional dependence of " $s-t$ ").

group similar to RE manganites. The polar Pn2_{1a} space group is sub-space group of nonpolar Pnma space group. Therefore, Rietveld refinement was carried out with dual phase model (R3c + Pn2_{1a}). For $x = 0.1$ composition, it is found that around 86% of rhombohedral R3c phase and remaining 14% that of orthorhombic Pn2_{1a} phase. Sample with $x = 0.15$ shows 42% of R3c and 58% of Pn2_{1a} phase, whereas $x = 0.2$, shows 24% of R3c and 76% of Pn2_{1a} phase. The transition from rhombohedral to a mix phase consists of rhombohedral plus orthorhombic phase is expected and can be explained by strong destabilization of R3c structure by Gd^{3+} due to chemical pressure

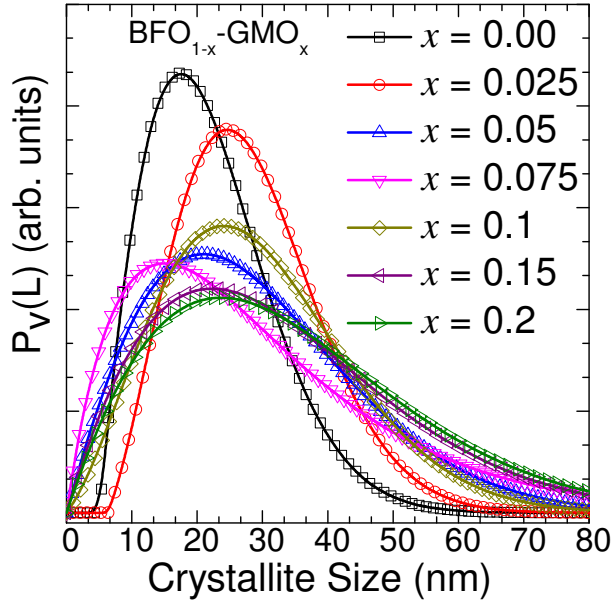


FIG. 3: Average crystallite size of $(\text{BFO})_{1-x}-(\text{GMO})_x$ $0.0 \leq x \leq 0.2$.

[17].

In order to establish the signature of compositional driven structural phase transition from $R3c$ to $R3c+\text{Pn}2_{1a}$, the pseudo-cubic lattice parameter as a function of composition was plotted in Fig. 2. Pseudo-cubic lattice parameter is defined as the cube root of the perovskite unit cell volume. It offers a convenient approach because it brings down lattice parameter to the same scale of magnitude for better understanding and is a suitable probe to analyze structural phase transition.

Figure 3 shows the average crystallite size of $(\text{BFO})_{1-x}-(\text{GMO})_x$ $0.0 \leq x \leq 0.2$ samples. The average crystallite size of the samples were calculated using Fourier X-ray line profile analysis (XLP) based on Double-Voigt method using the program package BREADTH [18]. The average crystallite size of $(\text{BFO})_{1-x}-(\text{GMO})_x$ $0.0 \leq x \leq 0.2$ solid solutions varies in the range 20 nm to 30 nm. To further support the XLP analysis, the microstructure of the sample $x = 0.2$ was investigated using high resolution transmission electron microscopy (HRTEM).

Fig. 4 shows the TEM micrograph (a) and selected area electron diffraction (SAED) pattern (b) of sample $x = 0.2$. The TEM micrograph (Fig. 4a) shows the average crystallite size of ~ 30 nm with some agglomeration, which agrees well with the average crystallite size obtained from XLP analysis. In order to get the structural insights and the presence of mixed phase, SAED pattern was taken for selected samples. Fig. 4(b) shows the SAED patterns of sample $x = 0.2$. The presence of set of ring diffraction patterns and absence of spotty diffraction patterns clearly show the polycrystalline nature of the sample. The indexing of diffraction pattern (Fig. 4(b))

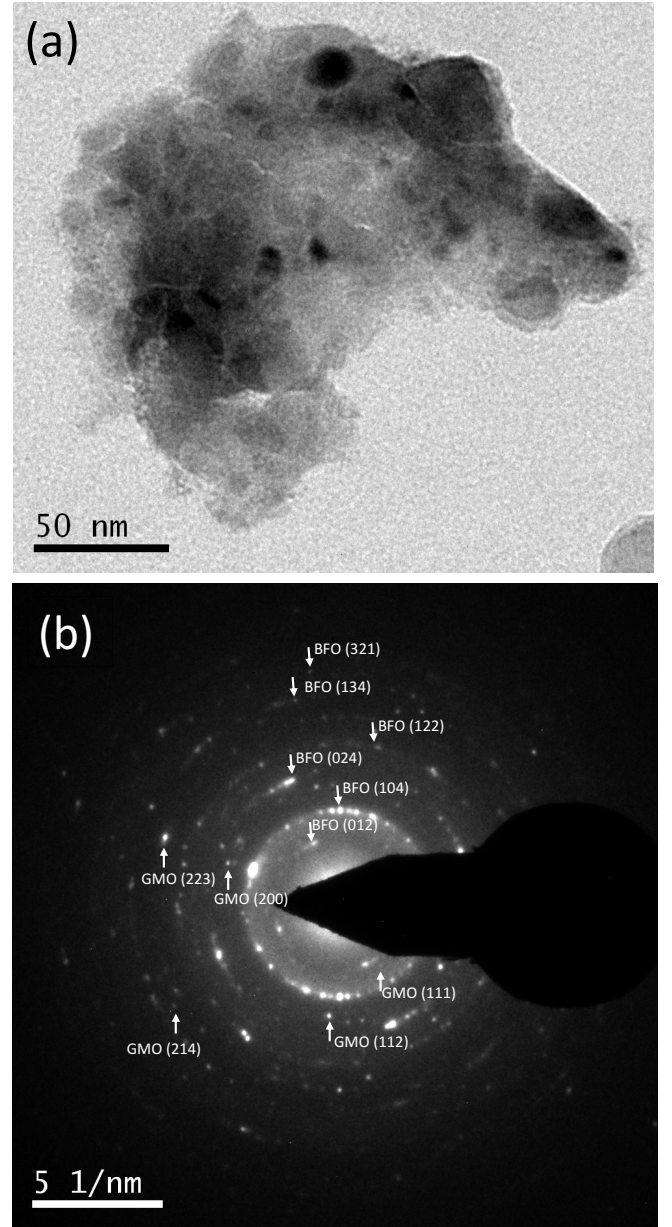


FIG. 4: Transmission electron microscopy (TEM) of $(\text{BFO})_{1-x}-(\text{GMO})_x$ $x = 0.2$: (a) TEM image showing nanoparticles of average size of 25 nm; (b) the selected area electron diffraction (SAED) pattern showing polycrystalline nature and mixed phase of the sample.

clearly shows the presence of mixed phases. This observation is in agreement with the XRD Rietveld refinement finding of the presence of the mixed $R3c+\text{Pn}2_{1a}$ phase in $x=0.2$ sample.

For better the understanding of microstructure, the fractured surface of the samples were analyzed with scanning electron microscope (SEM). Figure 5 shows the scanning electron micrographs of selected $(\text{BFO})_{1-x}-(\text{GMO})_x$ samples ($x = 0.0, 0.05, 0.1, \text{ and } 0.2$). As can

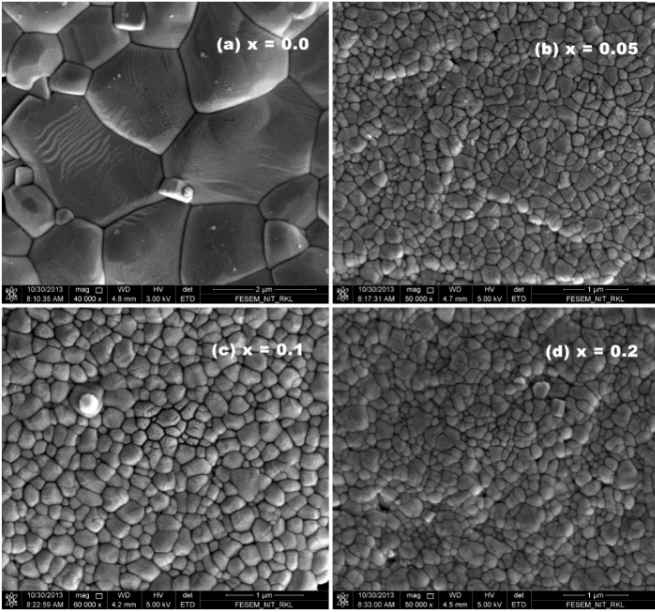


FIG. 5: SEM micrographs of $(\text{BFO})_{1-x}-(\text{GMO})_x$ solid solutions: (a) $x = 0.0$; (b) $x = 0.05$; (c) $x = 0.1$, and (d) $x = 0.2$.

be seen from the SEM micrographs, the samples show densely distributed grains with well defined grain boundary without defects and voids. Pure BFO (Fig. 5a) shows highly non-uniform grain size distribution ranging from 200 nm-2 μm , whereas samples with $x = 0.05, 0.1$, and 0.2 (Fig. 5b-d) show distribution of uniform grain size of average 200 nm. A decreasing in grain size was observed in solid solutions with increasing GMO concentration. This observation is not yet well understood, however, it can be attributed to the reduction of electrical resistivity due to the incorporation of rare earth oxide (GMO) phases into the semiconducting BFO phase which facilitate an enhanced diffusion process and decreasing grain size. The reduction in electrical resistivity by 10 orders of magnitude has been reported in BaTiO_3 with rare earth oxide incorporation [19].

B. Raman spectroscopy

In order to get the structural insight of the composition driven phase transition and changes in phonon response, micro-Raman spectra were recorded in backscattering geometry using Ar ion laser ($\lambda = 514.5 \text{ nm}$). Figure 6 shows the comparison of Raman spectra of $(\text{BFO})_{1-x}-(\text{GMO})_x$ $0.0 \leq x \leq 0.2$ samples at RT. According to the group theory selection rules, the rhombohedral structure of BFO with $R3c (C_{3v})$ symmetry will give rise to $4A_1 + 9E$ Raman active modes [5, 6]. The peaks at low temperature (81 K) in single domain single crystal observed at around 75, 265, 350, and 523 cm^{-1} are assigned as A_1 modes, whereas peaks at around 79, 145, 175, 224, 277, 295,

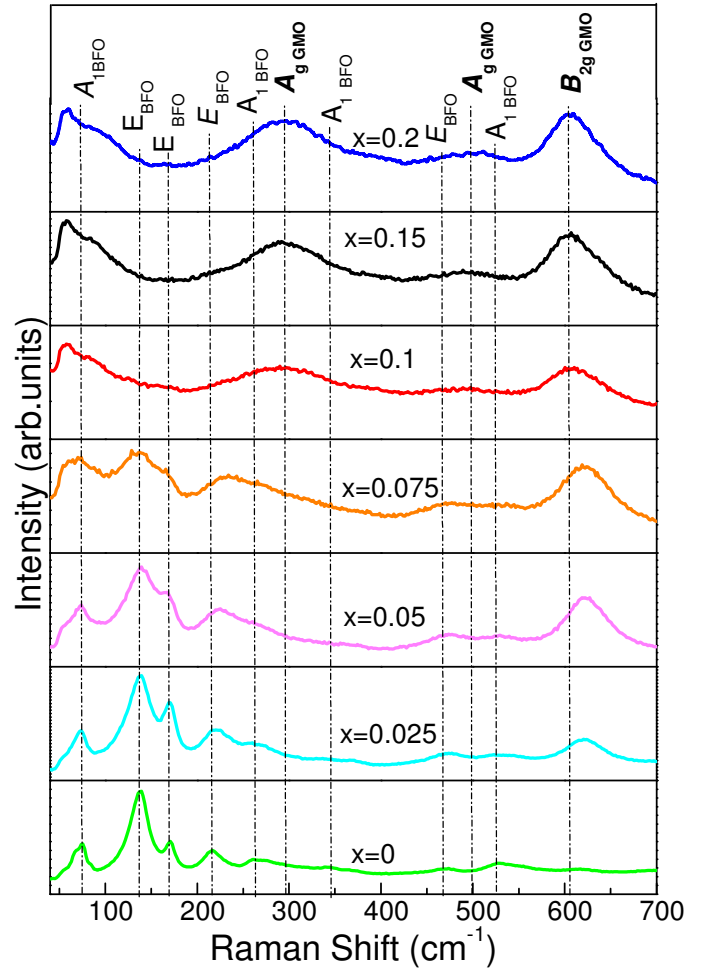


FIG. 6: Raman spectra of $(\text{BFO})_{1-x}-(\text{GMO})_x$ $0.0 \leq x \leq 0.2$ solid-solutions. The vertical dotted lines in the figure are a guide to the eye.

371, 473, and 553 cm^{-1} are assigned as E modes [6]. Of these 13 single phonon modes of BFO, we observed only eight Raman active modes in $(\text{BFO})_{1-x}-(\text{GMO})_x$ $0.0 \leq x \leq 0.2$ samples at RT. Some modes are not seen due to thermal broadening effect at RT. As can be seen from the Fig 6, the A_1 modes are observed at around 75, 262, 344, and 530 cm^{-1} , whereas, four E modes are seen at around 139, 171, 370 and 470 cm^{-1} in agreement with BFO single crystal Raman spectra [5, 6].

As GMO concentration increases, we observed some suppression of BFO phonon modes and appearance of three new phonon modes at around 293, 497, and 620 cm^{-1} associated with GMO. The peak at 620 cm^{-1} (B_{2g} (1) mode) appears from $x = 0.025$ is associated with the in-plane O_2 stretching and called as breathing mode. This mode is shifting to higher frequency with increasing GMO concentration. The mode at 293 cm^{-1} (A_g (2) mode) appears from the sample $x = 0.1$ is related to the in-phase rotation (y -axis) of MnO_6 octahedra and O_2 motion along x -axis. The mode at around 497 cm^{-1}

(A_g (3) mode) appears in samples $x \geq 0.15$ corresponds to bending of MnO_6 octahedra and O_2 anti-stretching [20]. As can be seen from Figure 6, it is quite evident that $(\text{BFO})_{1-x}$ - $(\text{GMO})_x$ up to $x = 0.075$ show phonon features dominated by BFO phase, while samples with higher concentration of GMO ($x \geq 0.1$) show phonon anomalies indicating the existence of mixed structural phase. The observation of mixed phase at higher concentration of x agrees well with the XRD and TEM (SAED) studies.

C. Dielectric Properties

In order to understand the dielectric behavior, the dielectric permittivity (ϵ), dielectric loss ($\tan \delta$), conductivity (σ_{ac}), and phase angle (θ) were measured as a function of frequency and temperature. Figure 7(a) shows the frequency variation of dielectric permittivity. The observation of decrease in permittivity with increasing frequency is the typical behavior of ferroelectrics. The high dielectric permittivity observed at low frequency can be explained by the presence of a potential barrier probably due to the existence of space charge polarization at the grain boundaries. This can lead to the accumulation of charges at the grain boundary, which leads to the high value of dielectric permittivity [21–23]. The decrease in dielectric permittivity with increasing frequency can be attributed to the reduction of space charge polarization [23]. The change in dielectric dispersion behavior (non-exponential) with increasing polar phase ($\text{Pn}2_{1a}$) upon GMO substitution can be attributed to the presence of morphotropic phase boundary (MPB). No significant change is observed on the values and nature of dielectric dispersion at higher frequencies. However, at low frequency (< 1 kHz) an increase in dielectric permittivity was observed with increasing GMO concentration. This can be explained by the change in conductivity or dipole relaxation phenomena [19].

To understand the nature of dielectric relaxation process, the dielectric dispersion behavior was analyzed with various dielectric relaxation models. As can be seen, the data fits very well with the modified Maxwell-Wagner (MW) relaxation model, as described in Equation 1 [24–26]:

$$\epsilon'(f) = \epsilon_\infty + \frac{1}{2}(\epsilon_s - \epsilon_\infty)b + Af^{-n} \quad (1)$$

$$b = 1 - \frac{\sinh[(1-\alpha)\ln(2\pi f\tau)]}{\cosh[(1-\alpha)\ln(2\pi f\tau + \sin(\frac{1}{2}\alpha\pi))]},$$

where ϵ_s is the dielectric permittivity at the lowest frequency, ϵ_∞ is the dielectric permittivity at the highest frequency, α is the measure of the polydispersity of the system, τ is the total relaxation time, and n is the dispersion parameter of frequency [27, 28]. The main consideration of the MW effect is the charge accumulation

TABLE II: Fitting parameters obtained from Maxwell-Wagner model for $(\text{BFO})_{1-x}$ - $(\text{GMO})_x$ $0.0 \leq x \leq 0.2$ at RT for dielectric permittivity at lower frequencies (ϵ_s) dielectric constant at higher frequencies (ϵ_∞), polydispersity (α), dispersion parameter of frequency (n), and the relaxation time (τ).

| x | ϵ_s | ϵ_∞ | α | n | τ (ms) |
|-------|--------------|-------------------|----------|------|-------------|
| 0.0 | 220 | 37 | 0.43 | 0.59 | 0.19 |
| 0.025 | 142 | 45 | 0.45 | 0.55 | 0.24 |
| 0.05 | 144 | 42 | 0.57 | 1.0 | 0.29 |
| 0.075 | 185 | 35 | 0.81 | 1.0 | 0.39 |
| 0.1 | 396 | 41 | 0.82 | 1.0 | 0.72 |
| 0.15 | 461 | 67 | 0.63 | 0.98 | 0.73 |
| 0.2 | 688 | 67 | 0.48 | 1.0 | 0.75 |

at the interface and their different charge carrier relaxation times [24]. The MW effect is commonly observed in two-material interface, such as metal-insulator, metal-semiconductor, insulator-semiconductor, semiconductor-semiconductor, *etc* [24, 27, 28]. The ratio of dielectric constant to conductivity is the relaxation time associated with the spreading of the excess free carriers in the materials [24]. The *solid line* in Fig. 7a shows fits of the modified Maxwell-Wagner relaxation model with the experimentally observed data. The values of ϵ_s , ϵ_∞ , α , n , and τ obtained from the MW-model for $(\text{BFO})_{1-x}$ - $(\text{GMO})_x$ ($0.0 \leq x \leq 0.2$) solid solutions at RT are given in Table II. As can be seen, the relaxation time increases with increasing x . A significant increase in relaxation time was observed for samples with $x \geq 1$, which can be associated with the increase of polar phase and MPB.

Figure 7(b) shows the frequency variation of dielectric loss of BFO-GMO solid solutions. As can be seen, samples with $x \leq 0.05$ show low dissipation compared to BFO in the measured frequency range. The sample with $x = 0.075$ shows low loss at higher frequencies compared to BFO. Samples with $x \geq 0.1$ show no improvement in dielectric dissipation at lower frequencies, but shows slightly higher loss at higher frequencies.

The ac conductivity (σ_{ac}) of the $(\text{BFO})_{1-x}$ - $(\text{GMO})_x$ samples obtained from the dielectric measurements using the formula [29, 30] $\sigma = \sigma_0 \omega \epsilon_0 \epsilon \tan \delta$, where σ_0 is the frequency independent conductivity, ω is angular frequency, ϵ_0 is vacuum dielectric permittivity, is shown in Figure 7(c). Generally, σ_{ac} of dielectrics increases with increasing both the frequency and the temperature. The frequency variation of ac conductivity was analyzed by universal power law proposed by Jonscher [31]: $\sigma_{ac} = A\omega^n$. This power law is related to the dynamics of the ionic hopping transport between localized sites. The exponent n is the measure of the degree of interaction with the materials conduction environment. The exponent in the range of 0.6-1.0 indicates disordered or amorphous systems and the conduction mechanism is mostly associated with diffusion limited hopping. Exponent $n \approx 1$ implies ideal long-rang (band-to-band) conduction process, which is normally observed at low temperature, whereas $n > 1$ indicates the presence of ther-

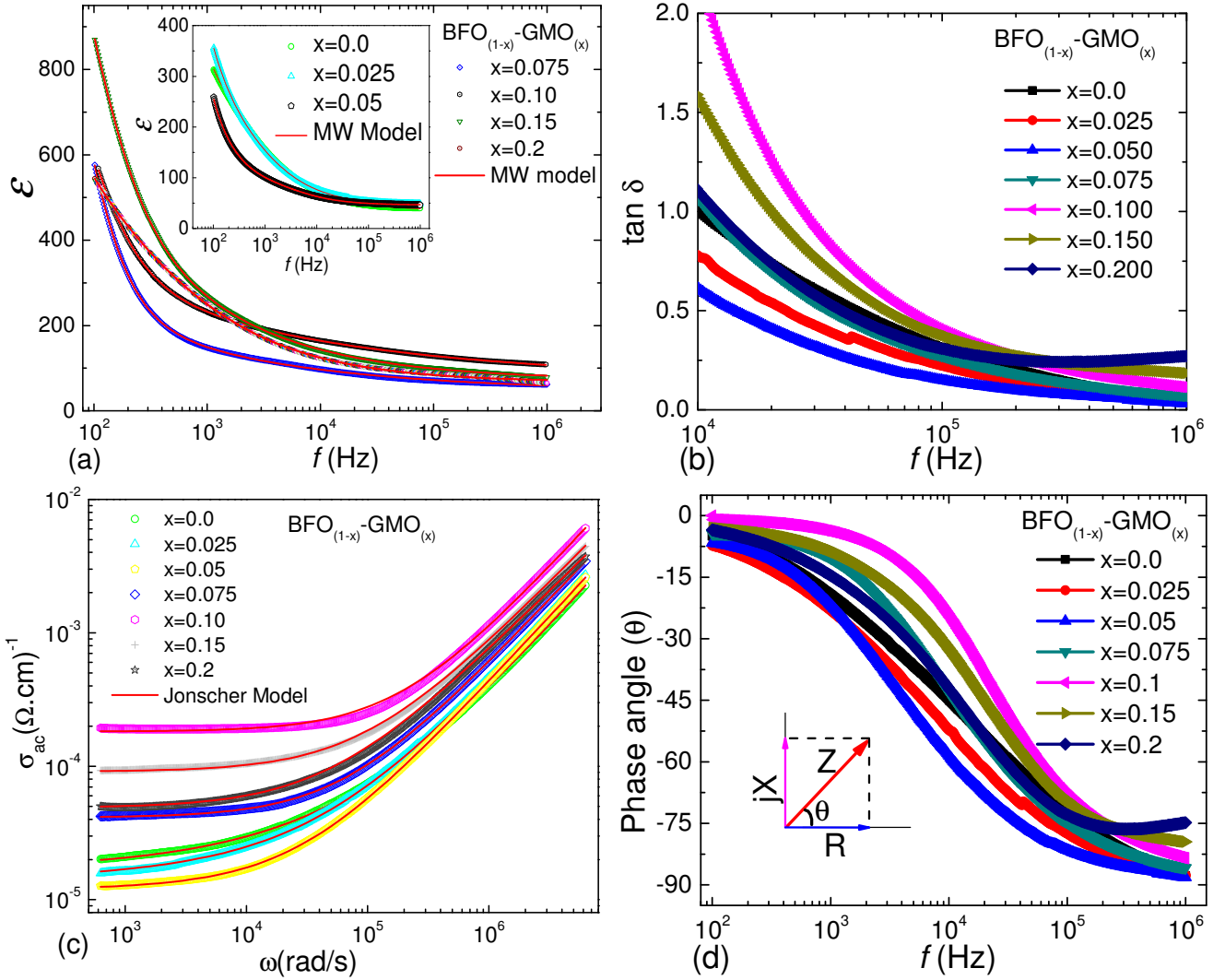


FIG. 7: Dielectric properties of $(\text{BFO})_{1-x}(\text{GMO})_x$ $0.0 \leq x \leq 0.2$ as a function of frequency at RT: (a) Dielectric permittivity (ϵ); (b) Dielectric loss ($\tan \delta$); (c) ac conductivity (σ_{ac}); (d) phase angle (θ), the angle between the real part (Resistance, R) and imaginary part (Reactance, X) of impedance (cf. inset). The *solid-line* in (a) and (c) shows the Maxwell-Wagner (MW) model and Jonscher Model fit to the data, respectively.

mally activated hopping process between two sites separated by energy barrier [29]. It also could be due to the presence of two dispersion processes with different relaxation times [32–35]. As can be seen, the ac conductivity σ_{ac} shows an excellent fit (solid line) to the modified Jonscher model, as defined in Equation 2 [29, 31]:

$$\sigma_{ac}(\omega) = \sigma_0 + A_1\omega^{n_1} + A_2\omega^{n_2}, \quad (2)$$

where σ_0 is the frequency independent conductivity (dc conductivity), A_1 and A_2 are the coefficients, and n_1 and n_2 are critical exponents. The universal power law was modified with hopping relaxation model and conduction through grain boundaries. The first exponent is associated with the charge carriers motion due to dc conduction

TABLE III: Fitting parameters obtained from the modified Jonscher power law model for $(\text{BFO})_{1-x}(\text{GMO})_x$ ($0.0 \leq x \leq 0.2$) solid solutions at RT.

| x | $\sigma_{dc} \times 10^{-5}$ ($\Omega \text{ cm}$) ⁻¹ | $A_1 \times 10^{-9}$ | $A_2 \times 10^{-10}$ | n_1 | n_2 |
|-------|---|----------------------|-----------------------|-------|-------|
| 0.0 | 1.69 | 131 | 1.15 | 0.48 | 1.06 |
| 0.025 | 1.38 | 152 | 3.07 | 0.42 | 1.02 |
| 0.05 | 1.11 | 342 | 5.19 | 0.18 | 0.98 |
| 0.075 | 4.13 | 0.21 | 6.65 | 0.97 | 0.97 |
| 0.1 | 1.83 | 0.52 | 4.66 | 0.99 | 0.99 |
| 0.15 | 9.12 | 1.05 | 10.5 | 0.93 | 0.93 |
| 0.2 | 4.89 | 1.46 | 14.7 | 0.90 | 0.90 |

and dispersive ac response. The frequency at which slope changes is known as hopping frequency of the polarons (ω_p) and is temperature dependent. The plateau region

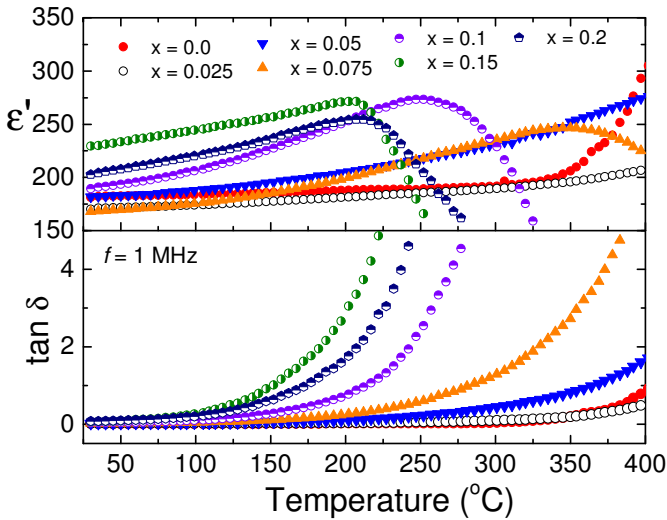


FIG. 8: Temperature variation of dielectric permittivity (a) and loss (b) of $(\text{BFO})_{1-x}-(\text{GMO})_x$ $0.0 \leq x \leq 0.2$ solid-solutions.

corresponds to the frequency-independent dc conductivity. The rise in the conductivity value with frequency indicates a normal ferroelectric behavior [36]. The conduction parameters and critical exponents obtained from the fitting are given in Table III. As can be seen, n_1 varies from 0.48 to 0.90 and n_2 varies from 0.90 to 1.06 indicating presence disordered phase and hopping type conduction process. The different n could be indicative of the charge carriers might have translational motion with a sudden hopping and localized hopping [37].

Figure 7(d) shows the frequency variation of phase angle (θ), the angle between the real (resistance, R) and imaginary part (reactance, X) of impedance $Z = R + jX$, of BFO-GMO samples. All the samples show a resistivity behavior at low frequency and gradually changes to highly capacitive nature at higher frequencies, which is consistent with the observation of very low dielectric dissipation at high frequency.

Fig. 8 shows the temperature variation of dielectric permittivity (ϵ_r) and loss ($\tan \delta$) of $(\text{BFO})_{1-x}-(\text{GMO})_x$ $0.0 \leq x \leq 0.2$ at $f=1$ MHz. The dielectric permittivity (Fig.8a) pure BFO shows an anomaly at around the Neel temperature ($T_N = 360^\circ\text{C}$). Samples with $x=0.025$ and 0.05 show behavior similar to BFO showing a very weak anomaly near magnetic transition temperature. However, samples with higher concentration of GMO ($x \geq 0.1$) show the shifting of anomaly towards lower temperature. Samples with $x=0.075, 0.10, 0.15,$ and 0.2 show anomaly at around $345, 275, 206,$ and 212°C , respectively. The observation of the shifting of the anomaly implies the shifting of the magnetic phase transition of the BFO towards the lower temperature. The dielectric loss (Fig.8b) as a function of temperature shows similar anomaly with increasing x . For pure BFO, the loss was almost constant up to T_N and above T_N it shows very

slow increase. As the concentration of x increased in the solid solution the anomaly of dielectric loss shifted towards lower temperature with faster rate. The observed behavior of dielectric permittivity and loss in BFO is consistent with the reported results [38].

D. Ferroelectric Properties

Figure 9 shows the ferroelectric polarization of some unpolled $(\text{BFO})_{1-x}-(\text{GMO})_x$ ($x=0.0, 0.025,$ and 0.05) samples at RT. The absence of saturation of polarization implies the lossy ferroelectric behavior. Decreasing in remanence and coercivity was found with increasing GMO concentration. Samples with higher concentration of $x (> 0.05)$ show very similar PE loop as sample $x=0.05$. The observed polarization is very low compared to the values obtained in single crystal and thin film, but it agrees well with the polycrystalline samples [38]. The polarization in BFO is associated with the Bi $6s$ lone pair electrons. However, the high polarization observed in thin films is attributed to the large strain-induced Fe-ion displacement relative to the oxygen octahedra in addition to the contribution of Bi $6s$ lone pair electrons [39]. The polarization in BFO is also highly dependent on structural phase [39]. The observation of suppression of polarization is attributed to the domain wall pinning [40]. BFO has very complex domain structures (twin 71° , twin 109° , and twin 180° domain walls) [40]. In polycrystalline samples, disorders play a significant role in suppressing polarization. Polycrystalline samples could not sustain the high electric field required for switching the magnetization to study the magnetoelectric effect. So, we focused our magnetoelectric (ME) coupling studies through magnetodielectric effect.

E. Magnetic Properties

Figure 10 shows the magnetic hysteresis loop of $(\text{BFO})_{1-x}-(\text{GMO})_x$ ($0.0 \leq x \leq 0.2$) solid solutions at RT (300 K) and 2 K. As can be seen from the RT hysteresis loop (Fig. 10(a)), pristine BFO and BFO with 2.5% GMO shows no hysteresis loop even up to field of 2 T. This observation is in agreement with the nature BFO magnetic ordering [1, 2]. The magnetic nature of BFO is associated with the canted G-type antiferromagnetic ordering with spiral spin modulation of 60 nm [41], due to the combined effect of exchange interaction and spin-orbit coupling. In the case of GMO, the ferromagnetically ordered Gd ($T_c=293$ K) spins significantly contribute to the net magnetic moment compared to the antiferromagnetically canted state of Mn ($T_N=100$ K) spins [15]. The solid solutions with higher concentration of x show ferromagnetic-like hysteresis loop at RT. This could be due to the change in magnetic ordering in BFO from the cycloidal spiral spin structure to a ferromagnetic ordering with increasing GMO concentration. Relatively high value of reman-

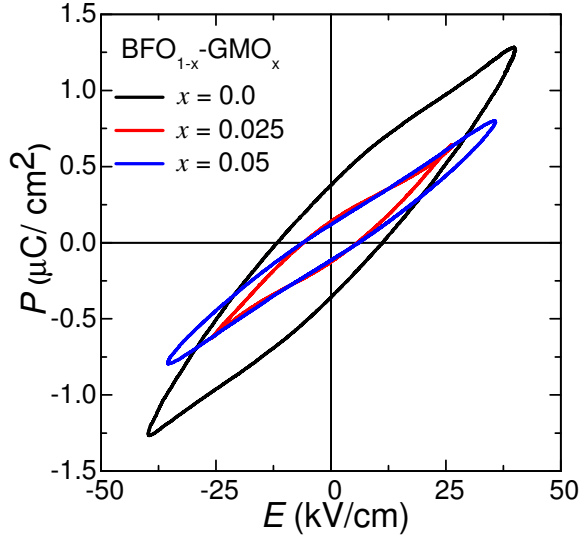


FIG. 9: Ferroelectric polarization of $(\text{BFO})_{1-x}(\text{GMO})_x$ ($x = 0.0, 0.025, \text{ and } 0.05$) solid solutions.

ment magnetization and coercivity was observed in BFO with 10% GMO compared to other samples. The inset in Fig. 10(a) shows the variation of coercivity (H_c) and remanent (M_r) magnetization as the function of x at RT.

Figure 10(b) shows the MH loop at 2 K. As can be seen, no magnetic hysteresis is observed for pure BFO, which is consistent with its intrinsic magnetic ordering. We observed higher magnetization and saturation at 2 K in other samples and the trend is somewhat commensurate with the RT observation that the sample $x = 0.1$ shows higher coercivity compared to other samples. The improved magnetization and coercivity observed in samples with $x \leq 1.0$ can be attributed to the synthesis of nano-crystalline solid solutions of BFO-GMO which might have introduced strain leading to the suppression of spin cycloid modulation of BFO and appearance of uncompensated spins [41–43]. The following possibilities might be responsible for the observed effect: (i) substitution of Gd^{3+} at Bi-site might have facilitated to collapse of space modulated spin structure; (ii) substitution of magnetically active Mn^{3+} at Fe-site of BFO favors ferromagnetic interaction. It is well known that the magnetic properties can be affected significantly by the nearest and next nearest neighbor exchange interactions. The samples with higher doping concentration GMO concentration ($x \geq 0.15$) shows reduction in coercivity and remanence, which can be explained by the change in neighboring magnetic ions ordering from ferromagnetic to an antiferromagnetic (substitution of ferromagnetic spins of Fe by antiferromagnetic spin of Mn). This can reduce the exchange interactions resulting in lower magnetization.

In order to understand the nature of magnetic ordering and magnetization dynamics, temperature variation of field cooled (FC) and zero field cooled (ZFC) magnetization was carried out from RT down to 2 K

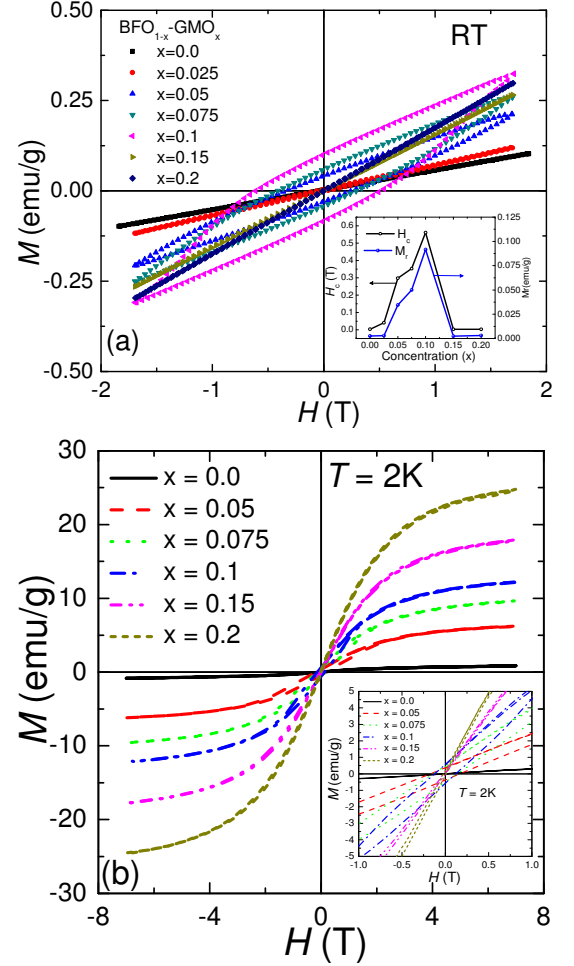


FIG. 10: MH loop of $(\text{BFO})_{1-x}(\text{GMO})_x$ ($0.0 \leq x \leq 0.2$) solid solutions: (a) room temperature (300 K); (b) 2 K.

as shown in Figure 11. As can be seen, the FC and ZFC magnetization show very similar behavior indicating the absence of secondary magnetic phase and magnetic frustrations [44]. The sharp increase of magnetization at low temperature could be related to the presence of paramagnetic cluster or phase [45, 46]. Since the $4f$ electrons of the rare earth (Gd^{3+}) are very localized, the direct exchange is not a dominating mechanism for the magnetic properties [45, 46]. According to the Goodenough-Kanamori-Anderson (GKA) rules [47–50], the strong superexchange interaction between Mn^{3+} and Mn^{4+} through oxygen (O^{2-}) anion (magnetic ion-ligand-magnetic ion are in 180°) results in antiferromagnetic ordering, whereas, a 90° superexchange interaction between $\text{Mn}^{3+}/\text{Mn}^{3+}$ and $\text{Mn}^{3+}/\text{Mn}^{4+}$ through vacancies could result in weaker ferromagnetic ordering. The antiferromagnetic coupling between Mn atoms is energetically favored [50]. The observation of ferromagnetic-like behavior and non-saturation of magnetization at low temperature in BFO-GMO solid solution samples could be due to the presence of both the types of superex-

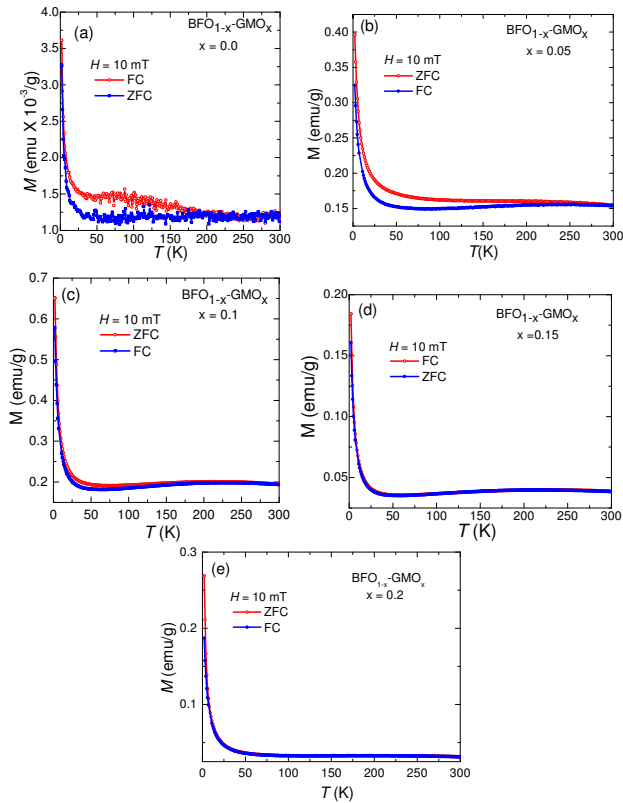


FIG. 11: Temperature variation of ZFC and FC magnetization of loop of $(\text{BFO})_{1-x}(\text{GMO})_x$: (a) $x = 0.0$; (b) $x = 0.05$; (c) $x = 0.10$; (d) $x = 0.15$; (e) $x = 0.20$.

changes.

F. Magnetodielectric properties

1. Impedance and Modulus Spectroscopy

The dynamical features of dielectrics and ferroelectrics are accompanied by the motion of charges, *e.g.* orientation polarization of dipoles and/or the motion of ions. Impedance (Z) and modulus (M) spectroscopy are powerful methods of characterizing the electrical properties of materials and their interface with electrodes. The impedance spectroscopy (IS) allows the separation of resistances related to grains, grain boundaries, and electrode effects because of their different relaxation times that results in a separate semicircles in impedance spectra [26]. These techniques can also be used to study the dynamics of bound or mobile charge in the bulk or interfacial regions of solids and provide a better insight for understanding the relationship between electrical transport and microstructure in nanocrystalline samples.

In order to understand the dielectric relaxation, *e.g.* long-range conductivity (non-localized) and dipolar (localized) relaxation, we carried impedance spectroscopy

of multiferroic solid solutions with and without magnetic field (H). Figure 12 shows the Nyquist plot of real (Z') and imaginary (Z'') part of the impedance of $(\text{BFO})_{1-x}(\text{GMO})_x$ ($0.025 \leq x \leq 0.2$) solid solutions as a function of magnetic field at RT. As can be seen, the sample with $x=0.025$ (Fig. 12a) shows a non-linear behavior, but not semicircular, suggesting an insulating nature. The undoped BFO (not shown) shows very similar behavior as in the case BFO with 2.5% of GMO. The semicircular behavior gradually develops with increasing concentration of x . For $x=0.05$, a semicircular arc starts forming and became prominent with increasing composition up to $x=0.075$. Samples with composition $x \geq 0.1$, exhibit the presence of two overlapping semicircular arcs with their centers below the real axis. The high frequency semicircle is attributed to the bulk (grain) property of the material, whereas the low frequency semicircular arc observed at intermediate frequency is attributed to the grain boundary effect. The intercept of the semicircular arcs on the real axis gives rise to grain and grain boundary resistance of the materials. The absence third semicircle rules out the presence of electrode-sample interface effect. As can be seen, all the samples show suppression in resistance with increasing magnetic field.

For quantitative understanding of the impedance behavior and the effect of grain and grain boundary contributions, the data were simulated with the equivalent circuit using a *brick-layer model* for a polycrystalline material [26]. The high frequency semicircular arc was modeled to an equivalent circuit shown in inset Figure 12a. The equivalent circuit contains parallel combination of a bulk resistance (R_1), bulk capacitance (C_1) along with a constant phase element (CPE) [26], whereas the low frequency semicircular arc was modeled for parallel combination of grain boundary resistance (R_2) and grain boundary capacitance (C_2). The CPE admittance is $Y(\text{CPE}) = A_0(j\omega)^n = A\omega^n + jB\omega^n$ [26], where $A = A_0 \cos(n\pi/2)$ and $B = A_0 \sin(n\pi/2)$. A_0 and n are frequency independent parameters usually depend on temperature, A_0 determines the magnitude of the dispersion and the n value is $0 \leq n \leq 1$ [17]. The CPE describes an ideal capacitor for $n=1$ and an ideal resistor for $n=0$ [51–53]. Both the equivalent circuits are connected in series for fitting the impedance data. The *solid line* in Figure 12 shows simulated fit of equivalent circuit to the data using an electrochemical impedance spectroscopy (EIS) data analysis software (ZSimpWin) [54]. As can be seen, a good agreement has been found with the equivalent circuit simulated data with the observed data. Tables IV and V list the bulk capacitance and resistance, respectively, obtained from the Nyquist fittings using the equivalent circuits (Inset Fig. 12a) for $(\text{BFO})_{1-x}(\text{GMO})_x$ ($0.0 \leq x \leq 0.2$) solid solutions. It is observed that for all the compositions the bulk capacitance decreases with increasing magnetic field, while bulk resistance increases, which indicates the presence of magnetoelectric coupling in BFO-GMO solid solutions.

For the better understanding of the relaxation process

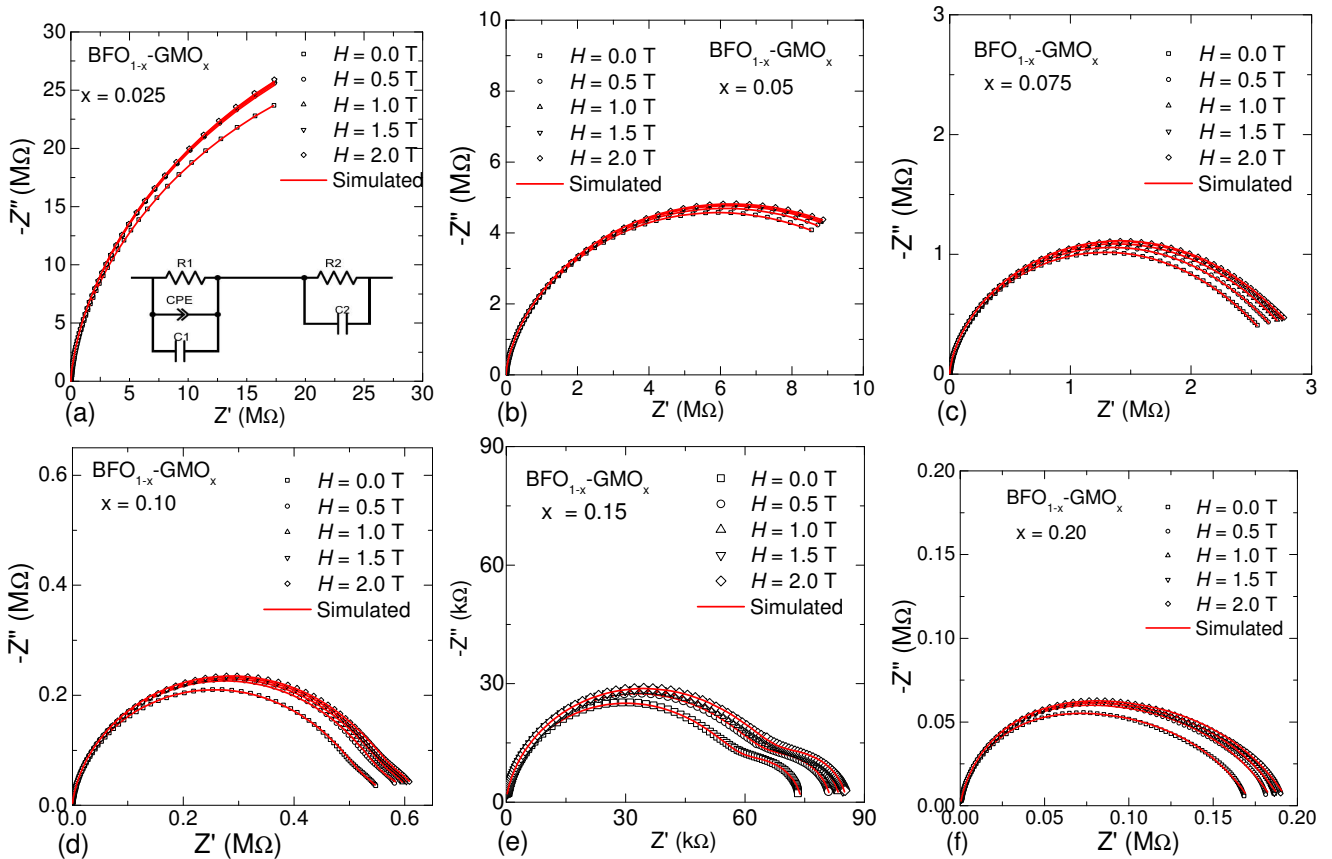


FIG. 12: Nyquist plot of $(\text{BFO})_{1-x}(\text{GMO})_x$ with different percentage of x ; (a) $x = 0.025$; (b) $x = 0.05$; (c) $x = 0.075$; (d) $x = 0.10$; (e) $x = 0.15$; (f) $x = 0.2$. The inset in (a) shows the equivalent circuit consisting of grain and grain boundary effect that was used to simulate the observed data.

TABLE IV: Bulk capacitance obtained from fitting of magnetic field dependent complex impedance plot of $(\text{BFO})_{1-x}(\text{GMO})_x$ ($0.0 \leq x \leq 0.2$) at RT.

| Bulk Capacitance (10^{-11} F) | | | | | | | |
|----------------------------------|-------|---------|--------|---------|-------|--------|-------|
| H(T) | x=0.0 | x=0.025 | x=0.05 | x=0.075 | x=0.1 | x=0.15 | x=0.2 |
| 0.0 | 4.174 | 2.783 | 3.578 | 3.258 | 3.544 | 6.305 | 5.788 |
| 0.5 | 4.145 | 2.734 | 3.320 | 3.188 | 3.490 | 6.286 | — |
| 1.0 | 4.152 | 2.733 | 3.319 | 3.187 | 3.400 | 6.193 | 5.562 |
| 1.5 | 4.152 | 2.734 | 3.320 | 3.186 | 3.380 | 6.184 | 5.559 |
| 2.0 | 4.152 | 2.732 | 3.316 | 3.178 | 3.400 | 6.188 | 5.545 |

TABLE V: Bulk resistance obtained from fitting of magnetic field dependent complex impedance plot of $(\text{BFO})_{1-x}(\text{GMO})_x$ ($0.0 \leq x \leq 0.2$) at RT.

| Bulk Resistance (Ω) | | | | | | | |
|------------------------------|--------|---------|--------|---------|--------|--------|--------|
| H(T) | x=0.0 | x=0.025 | x=0.05 | x=0.075 | x=0.1 | x=0.15 | x=0.2 |
| | 10^6 | 10^7 | 10^7 | 10^6 | 10^5 | 10^4 | 10^5 |
| 0.0 | 8.6176 | 8.238 | 1.226 | 2.522 | 5.415 | 6.240 | 1.307 |
| 0.5 | 9.3114 | 8.812 | 1.358 | 2.671 | 5.761 | 6.841 | 1.394 |
| 1.0 | 13.469 | 8.897 | 1.379 | 2.749 | 5.834 | 7.021 | 1.428 |
| 1.5 | 14.609 | 8.978 | 1.387 | 2.792 | 5.892 | 7.106 | 1.446 |
| 2.0 | 15.589 | 9.007 | 1.395 | 2.819 | 5.965 | 7.159 | 1.459 |

and dominating charge transport mechanisms, the dispersion of imaginary part of impedance (Z'') and modu-

lus (M'') of $(\text{BFO})_{1-x}(\text{GMO})_x$ ($0.025 \leq x \leq 0.2$) were measured and compared at a constant magnetic field (2 T) as shown in Figure 13. As can be seen, no relaxation peak (maxima) was observed for $x = 0.025$ (Fig. 13a), while samples with $x \geq 0.05$ (Fig. 13b-e) shows dielectric relaxation in both impedance and modulus. It was found that the relaxation time ($\tau = 1/2\pi f_{max}$, where f_{max} is the frequency corresponds to peak maximum of (Z'') and (M'')) decreases with increasing composition (x). The presence of dielectric relaxation peaks in impedance and modulus at different frequency implies non-Debye relation process which is dominated by the short-range hopping of charge carriers. In the case of long-range Debye type relaxation process the relaxation peak of impedance and modulus should appear at the same frequency [55–57]. Inserting a constant phase element modeled the observed impedance behavior very well.

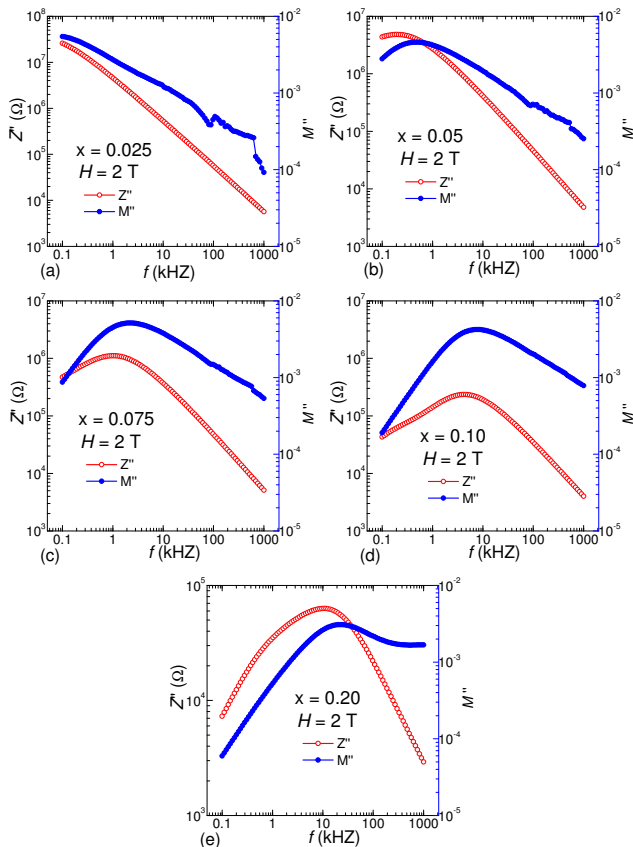


FIG. 13: Frequency dependent Z'' and M'' of $(\text{BFO})_{1-x}-(\text{GMO})_x$ with different percentage of x ; (a) $x = 0.0$; (b) $x = 0.025$; (c) $x = 0.05$; (d) $x = 0.075$; (e) $x = 0.10$.

2. Magnetocapacitance and Magnetoimpedance Measurement

In order to understand the magnetodielectric (MD) coupling, magnetocapacitance (MC) and magnetoimpedance (MI) of the BFO-GMO solid solutions were measured at RT. It has been predicted that an intrinsic magnetoresistance (MR) could enhance the MD effect from inhomogeneities. In ceramics the MR is dominated by the spin-polarized tunneling across the grain boundary. Maxwell-Wagner effect combined with MR could be the mechanism for magnetocapacitance without magnetoelectric coupling [58, 59]. To rule out the MR related MD coupling effect, we carry out frequency dependent MC and MI at RT.

The change in MC was measured with and without magnetic field as: $\text{MC}(H) = [C(H)-C(0)]/C(0)$, where $C(H)$ is the capacitance at the magnetic field H and $C(0)$ is the capacitance at the zero magnetic field. Figure 14 shows the MC of $(\text{BFO})_{1-x}-(\text{GMO})_x$ ($0.0 \leq x \leq 0.1$) solid solutions at 100 Hz and 1 kHz in forward and reverse magnetic field (0-2 T) sweeps. Our study was focused on the compositions away from the MPB. As can be

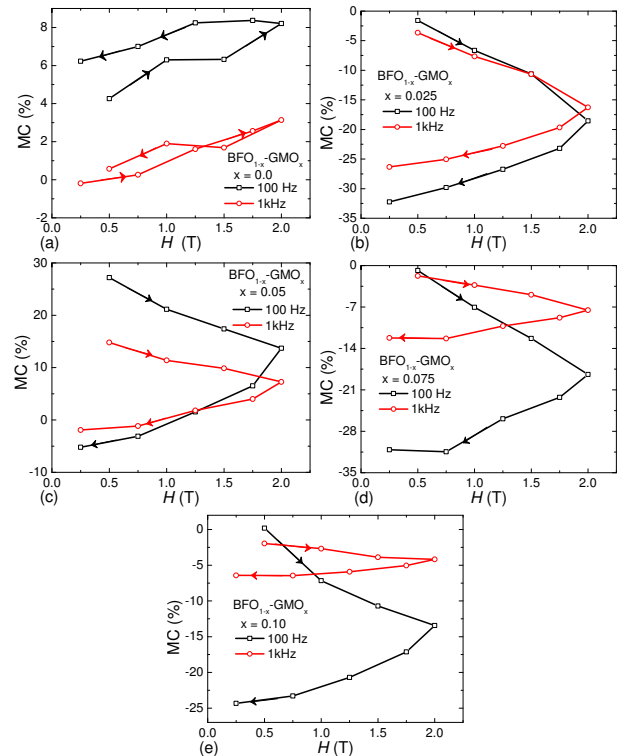


FIG. 14: Magnetocapacitance (MC) of $(\text{BFO})_{1-x}-(\text{GMO})_x$ with different percentage of x ; (a) $x = 0.0$; (b) $x = 0.025$; (c) $x = 0.05$; (d) $x = 0.075$; (e) $x = 0.10$.

seen, the undoped BFO (Figure 14a) shows very weak MC change and magnetic hysteresis, which agrees with its intrinsic magnetic ordering of BFO. Samples with $x=0.025, 0.05, 0.075$, and 0.10 (Figure 14b-e) shows about 20-25% MC and 25-30% magnetic hysteresis at 2 T and 100 Hz. A strong magnetodielectric (MD) effect could be useful for device applications. All the samples show reduced MC and hysteretic behavior at 1 kHz. The observed negative MC in samples with $x=0.025, 0.075$, and 0.10 in forward and reverse field sweeps indicates the presence of antiferromagnetic dominated magnetic ordering at RT. The sample with $x=0.05$ (Figure 14c) shows both the positive and negative MC change indicating the presence of both the ferromagnetic and antiferromagnetic orderings, which can be explained by the competing interaction between the ferromagnetically ordered Gd spins with the antiferromagnetically canted Mn spins. The observation of magnetic hysteresis shows the presence of long-range ordered magnetic states. BFO-GMO solid solutions shows significant enhancement in MC effect compared to the pure BFO, which can be explained the suppression of spin cycloidal structure in BFO as a result of GMO substitution.

To establish the existence of intrinsic MD coupling, we carry out frequency dependent magnetoimpedance (MI) at RT. Figure 15 shows MI of $(\text{BFO})_{1-x}-(\text{GMO})_x$ ($0.0 \leq x \leq 0.1$) solid solutions at 100 Hz and 1 kHz in forward

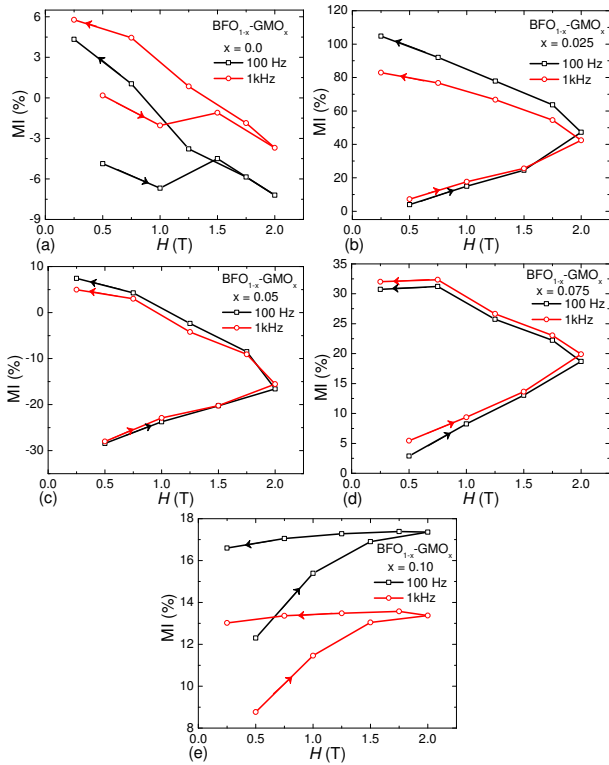


FIG. 15: Magnetoimpedance (MI) of $(\text{BFO})_{1-x}(\text{GMO})_x$ with different percentage of x : (a) $x = 0.0$; (b) $x = 0.025$; (c) $x = 0.05$; (d) $x = 0.075$; (e) $x = 0.10$.

and reverse magnetic field sweeps. The change in MI was measured with and without magnetic field as: $Z(H) = [Z(H) - Z(0)]/Z(0)$, where $Z(H)$ is the impedance at the magnetic field H and $Z(0)$ is the impedance at the zero magnetic field. BFO-GMO solid solution samples show significantly enhanced MI and magnetic hysteresis (Figure 15b-e) implying the existence of magnetodielectric coupling. The existence of magnetic hysteresis clearly indicates the presence of long range magnetic ordering. The undoped BFO shows (Fig. 15a) very small (2-3%) MI in forward magnetic field sweep at 2 T and 100 Hz and 1 kHz, while about 10% MI has been observed in reverse field sweep. Samples with $x=0.025$ (Fig. 15b) shows about 50% MI in forward field sweep, whereas about 60% MI observed in reverse field sweep. Samples with $x=0.05$ and 0.075 show about 15 and 20% MI in forward and reverse field sweep, respectively. Samples with $x=0.025-0.075$ (Fig. 15c-d) show very similar MI behavior with frequency and magnetic hysteresis. Sample with $x=0.10$ (Fig. 15e) shows about 4% MI in both forward and reverse field sweeps and the low MI effect can be explained due to the proximity of MPB. The observation of MC and MI at different frequencies clearly indicates the presence of enhanced magnetodielectric coupling in

BFO-GMO solid solutions.

IV. CONCLUSION

In summary, nanocrystalline solid solutions of $(\text{BFO})_{1-x}(\text{GMO})_x$ $0.0 \leq x \leq 0.2$ have been synthesized successfully by auto-combustion method. The analysis of structural property by Rietveld refinement showed the existence of morphotropic phase boundary at $x=0.10$, which is in agreement with the Raman spectroscopy and HRTEM studies. The dielectric dispersion behavior fits very well with the modified Maxwell-Wagner model. The frequency dependent phase angle study showed the resistive nature of solid solutions at low frequency, whereas it showed capacitive behavior at higher frequencies. The temperature variation of dielectric permittivity showed dielectric anomaly at magnetic phase transition temperature and it was shifted towards the lower temperature with increasing GMO concentration indicating the lowering of magnetic phase transition towards lower temperature. The Nyquist plot showed the conduction mechanism is mostly dominated by grains and grain boundary resistance. The ac conductivity of all the samples followed the modified Jonscher model. The impedance and modulus spectroscopy showed a non-Debye like relaxation mechanism which can be modeled using a CPE in the equivalent circuit. The unsaturated ferroelectric polarization loops indicated the lossy ferroelectric behavior. The BFO-GMO solid solutions showed enhanced ferromagnetic-like behavior at RT. The observation of frequency dependent magnetocapacitance and magnetoimpedance clearly showed the existence of an intrinsic magnetodielectric coupling. The $(\text{BFO})_{1-x}(\text{GMO})_x$ solid solutions with $x=0.025-0.075$ showed significantly high MC and MI compared to the pure BFO, which can be useful for practical device applications.

ACKNOWLEDGEMENTS

This work is supported by the National Science Foundation (NSF DMR-1410869). R. Masso and R. Martinez acknowledge the support received from NSF-PREM center (NSF-PREM-1827622).

DATA AVAILABILITY

The data that support the findings of this study are available from the corresponding author (R. Palai) upon reasonable request by email (r.palai@upr.edu).

-
- [1] Schmid H, 1994 *Ferroelectrics* **162** 317
- [2] Fiebig M Lottermoser T, Fröhlich D, Goltsev A V and Pisarev R V 2002 *Nature* **419** 818
- [3] Wang J, Neaton J B, Zheng H, Nagarajan V, Ogale S B, Liu B, Viehland D, Vaithyanathan V, Schlom D G, Waghmare U V, Spaldin N A, Rabe K M, Wuttig M and Ramesh R, 2003 *Science* **299** 1719
- [4] Palai R, Katiyar R S, Schmid H, Tissot P, Clark S J, Robertson J, Redfern S A T, Catalan G, and Scott J F, 2008 *Phys. Rev. B* **77** 014110
- [5] Palai R, Schmid H, Scott J F and Katiyar R S, 2010 *Phys. Rev. B* **81** 064110
- [6] Palai R, Scott J F, and Katiyar R S 2010 *Phys. Rev. B* **81** 024115
- [7] Hur N, Park S, Sharma P A, Ahn J S, Guha S and Cheong S W, 2004 *Nature* **429** 392-395
- [8] Scott J 2007 *Nat. Mater.* **6** 256-257
- [9] Pabst G W, Martin L W, Chu Y H, Ramesh R 2007 *Appl. Phys. Lett.* **90** 072902
- [10] Nagamuna H, Inoue Y and Okamura S 2007 *Integrated Ferroelectrics* **95** 242
- [11] Khomskii D 2009 *Physics* **2** 20
- [12] Schrettle F, Lunkenheimer P, Hemberger J, Ivanov V Y, Mukhin A A, Balbashov A M and Loidl A 2009 *Phys. Rev. Lett.* **102** 207208
- [13] Tripathy S N, Mishra K K, Sen S, Mishra B G, Pradhan D K, Palai R and Pradhan D K 2013 *J. Appl. Phys.* **114** 144104
- [14] Tripathy S N, Pradhan D K, Mishra K K, Sen S, Palai R, Paulch M, Scott J F, Katiyar R S Pradhan D K 2015 *J. Appl. Phys.* **117** 144103
- [15] Selbach S M, Tybell T, Einarsrud M and Grande T 2007 *Chem. Mater.* **19** 6478
- [16] Tripathy S N, Mishra B G, Shirolkar M M, Sen S, Das S R, Janes D B, and Pradhan D K, 2013 *Mater. Chem. Phys.* **141** 423
- [17] Tripathy S N 2014 *Ph. D Thesis* National Institute of Technology, Rourkela http://ethesis.nitrkl.ac.in/6680/1/Satya_N._Tripathy.pdf
- [18] Balzar D 1995 *J. Appl. Crystallogr.* **28** 244
- [19] Subbarao E C 1998 *Colloids and Surfaces A* **133** 3-11
- [20] Negi P, Dixit G, Agrawal H M, Kumar H, Srivastava R C, Sati P C, Gupta V and Asokan K 2017 *Ferroelectrics* **519** 200
- [21] Dar M A, Majid K, Batoo K M, and Kotnala R K, 2015 *J. Alloy Compd.* **632** 307-320
- [22] Rayssi C, Kossi S E, Dhahri J and Khirouni K 2018 *RSC Advances* **8** 17139
- [23] Alkathy M, James Raju K C and Eiras J A 2021 *J. Phys. D: Appl. Phys.* (in Press: <http://iopscience.iop.org/article/10.1088/1361-6463/abd12b>)
- [24] Iwamoto M 2015 *Maxwell-Wagner Effect* in Bhusan B. (Eds) *Encyclopedia of Nanotechnology* Springer, Dordrecht . DOI10.1007/978-94-007-6178-0_5-2
- [25] Shen M, Ge S and Cao W 2001 *J. Phys. D: Appl. Phys.* **34** 2935
- [26] Martinez, R, A Kumar, Palai R, Scott J F and Katiyar R S 2011 *J. Phys. D: Appl. Phys* **44** 105302
- [27] Clause M 1975 *Colloid Polym. Sci.* **253** 10204
- [28] Kamiyoshi K I, Fujimura T and Yamakami T, 1967 *Science reports of the Research Institutes, Tohoku University, Ser. A, Physics, chemistry and metallurgy*, **19** 125-152
- [29] Martinez R, Palai R, Huhtinen H, Liu J, Scott J F and Katiyar R S 2010 *Phys. Rev. B* **82** 134104
- [30] Alkathy M S and James Raju K C 2016 *J. Mater. Sci: Mater Electron* **27** 8957
- [31] Jonscher A K, 1977 *Nature* **264** 673
- [32] Pelai-Barranco A, Gutierrez-Amador M P, Huanosta A and Valenzuela R 1998 *Appl. Phys. Lett.* **73** 2039
- [33] James A R, Prakash C and Prasad G 2006 *J. Phys. D: Appl. Phys.* **39** 1635
- [34] Mahbood S, Prasad G and Kumar G S 2006 *Bull. Mater. Sci.* **29** 347
- [35] Macdonald J R 1997 *J. Non-Cryst. Solids* **210** 70
- [36] Das P S, Chakraborty P K, Behera B, Mohanty N K, Choudhary R N P 2014 *J. of Adv. Ceramics* **3** 1
- [37] Jump F K 1993 *Prog. Solid State* **22** 111
- [38] Wang T H, Ding Y, Tu C S, Yao Y D, Wu K T, Lin T C, Yu H H, Ku C S and Lee H Y 2011 *J. Appl. Phys.* **109** 07D907
- [39] Zhang J X *et al.*, 2011 *Phys. Rev. Lett.* **107** 147602
- [40] Park J W, Baek S H, Wu P, Winchester B, Nelson C T, Pan X O, Chen L Q, Tybell T and Eom C B 2010 *Appl. Phys. Lett.* **97** 212904
- [41] Park T, Papaefthymiou G C, Viescas A J, Moodenbaugh A R and Wong S S 2007 *Nano Lett.* **7** 766
- [42] Selbach S M, Tybell T, Einarsrud M, and Grande T, 2008 *Adv. Mater.* **20** 3692
- [43] Catalan G, Sardar K, Church N S, Scott J F, Harrison R J and Redfern S A T 2009 *Phys. Rev. B* **79** 212415
- [44] Palai R, Huhtinen H, Scott J F and Katiyar R S 2009 *Phys. Rev. B* **79** 104413
- [45] Dasari K, Wu J, Huhtinen H, Jadwisieniczak W M and Palai R 2017 *J. Phys. D: Appl. Phys.* **50** 175104
- [46] Dasari, Wang J, Guinel M J, Jadwisieniczak W M, Huhtinen H, Mundle R, Pradhan A K and Palai R, 2015 *J. Appl. Phys.* **118** 125707
- [47] Anderson P W 1959 *Phys. Rev* **115** 2
- [48] Anderson P W 1963 *Solid State Phys* **14** 99
- [49] Goodenough J B 1963 *Magnetism and the Chemical Bond*, John Wiley and Sons, New York
- [50] Geertsman W and Khomskii 1995 *Phys. Rev. B* **54** 3011
- [51] Raymond O 2005 *J. Appl. Phys.* **97** 084107
- [52] Schmidt R, Ventura J, Langenberg E, Nemes N M, Munuera C, Varela M, Hernandez M, Leon C and Santamaria J 2012 *Phys. Rev. B* **86** 035113
- [53] Gerhardt R 1994 *J. Phys. Chem. Solids* **55** 1491
- [54] <https://www.ameteksi.com/products/software/zsimpwin>
- [55] Sinclair D C and West A R 1989 *J. Appl. Phys.* **66** 3850
- [56] Morrison F D, Sinclair D C and West A R 1999 *J. Appl. Phys.* **86** 6355
- [57] Macdonald J R 2005 *Solid State Ionics* **176** 1961
- [58] Catalan G 2006 *Appl. Phys. Lett.* **88** 102902
- [59] Tang J, Feng L and Wiemann J A 1999 *Appl. Phys. Lett.* **74** 2522